Nano Research
2019, 12(8): 1921–1930

ISSN 1998-0124 CN 11-5974/O4
https://doi.org/10.1007/s12274-019-2459-8

Research Article

Function-regeneration of non-porous hydrolyzed-MOF-derived materials

Yo Chan Jeong[1], Jin Weon Seo[2], Jae Ho Kim[1], Seunghoon Nam[3], Min Chang Shin[2], Young Shik Cho[1], Jin Syul Byeon[2], Chong Rae Park[1] (✉), and Seung Jae Yang[2] (✉)

[1] *Carbon Nanomaterials Design Laboratory, Research Institute of Advanced Materials and Department of Materials Science and Engineering, Seoul National University, Seoul 08826, Republic of Korea*
[2] *Advanced Nanohybrids Lab., Department of Chemical Engineering, Inha University, Incheon 22212, Republic of Korea*
[3] *School of Advanced Materials Engineering, College of Engineering, Andong National University, Andong, Gyeongsangbuk-do 36729, Republic of Korea*

Received: 3 April 2019 / **Revised:** 22 May 2019 / **Accepted:** 5 June 2019

ABSTRACT

A facile synthetic strategy based on a water-based process is developed for the preparation of metal–organic framework (MOF)-derived materials by revisiting the hydrolyzed non-porous metal–organic frameworks (h-MOF). The poor water stability of MOF has been recognized as key limitations for its commercialization and large-scale applications because the hydrolysis resulted in the complete loss of their functionalities. However, we found that the negative effect of hydrolysis on MOF can be nullified during the heat treatment. As similar to the intact MOF, h-MOF can be used as a precursor for the preparation of MOF-derived materials from porous MOF-derived carbons (MDCs) to MDC@ZnO composites. The property of h-MOF-derived materials is almost equivalent to that of MOF-derived materials. In addition, h-MOF turned the weakness of water instability to the strength of facile water-based process for hybridization. With the demonstration of the hybrid composite between h-MDC@ZnO and reduced graphene oxide (rGO) as a prototype example, it exhibited superior electrochemical performance when evaluated as an electrode material for lithium-ion batteries.

KEYWORDS

nanomaterials, metal–organic framework (MOF), porous materials, MOF-derived carbon, hydrolyzed MOF

1 Introduction

Wide ranges of porous materials have been considered promising nanomaterials for future applications ranging from energy storage to drug delivery systems beyond their traditional use in ion exchange, adsorption, and catalysis [1, 2]. Among the various porous materials, metal–organic frameworks (MOFs) have been investigated widely owing to the versatility for modification of their nanostructures and hence, the properties of the nanomaterials [3–5]. Since the discovery of MOFs in the late 1990s, the ability to adjust the pore size of MOFs and tune the surface functional groups of the MOF surface are unique characteristics that have prompted considerable research in its applications in the areas of energy storage, drug delivery, selective sensing, and catalyst [6–15]. The relatively high synthetic yields of MOFs, including MOF-5, MOF-74, HKUST-1, or ZIF-8, make them promising for commercialization [16–18]. For example, a space-time yield (STY) of 2,000 $kg \cdot m^{-3} \cdot day^{-1}$ can be achieved, which allowed the large-scale production [18, 19].

Nevertheless, the limited stability of conventional MOFs under ambient atmospheric conditions remains a contentious issue because the MOFs are easily hydrated, resulting in the complete loss of their advantageous features [20]. Furthermore, the instability of MOFs within the water molecule severely limits the expandability of MOFs to the field of the nanocomposite synthesis, such as hybridization with graphene oxide (GO), carbon nanotubes (CNTs), and metal oxide nanoparticles, because they are usually prepared by a water-based synthetic process [21–24]. Considering increasing demands on MOF-carbon composites due to the widespread applications, improving the water stability of MOFs is the remaining key issue that needs to be addressed before the utility of MOFs and MOF derivatives can be expanded in various applications [25–27].

In general, MOFs are quite sensitive and degenerate easily under the infinitesimal traces of water molecules under ambient conditions [28, 29]. Moisture leads to the hydrolysis of MOF and hampers the original pore structure of MOFs [30]. Based on computational calculations, the framework begins to collapse at H_2O contents of 3.9% and O atoms are unable to be coordinated by Zn ions due to the replacement of the oxygen from the MOF with that from water according to the following mechanism: $(Zn_4O)(BDC)_3 + 4H_2O \rightarrow [Zn_4O](H_2O)_4(BDC)_2]^{2+} + BDC^{2-}$ [30]. The degradation of MOF by moisture exposure in the atmosphere was also experimentally investigated by Yang Ming et al. [31] and Rodríguez et al. [32].

Therefore, various efforts to enhance the water stability of MOFs have been made. A typical strategy is to introduce a protective layer, such as waterproof polydimethylsiloxane, as a hydrophobic layer of MOFs [28]. A carbon coating on the MOF surface is also an effective way to protect MOFs from hydrolysis [33]. These efforts are basically based on the long-held axiom that the water molecules severely degrade the MOF as supported by the drastic decrease in surface area. Hydrolysis leads to irreversible collapse of the pore structure of MOF, which renders hydrolyzed MOF impractical material for large scale applications.

On the other hand, it is unclear if it holds in cases of MOF-derived materials (c.f. MOF-derived carbons). The elements, Zn, O, and C, of MOFs are distributed atomically in both MOFs and even in hydrolyzed MOFs. Therefore, hydrolyzed MOFs might have

Address correspondence to Chong Rae Park, crpark@snu.ac.kr; Seung Jae Yang, sjyang@inha.ac.kr

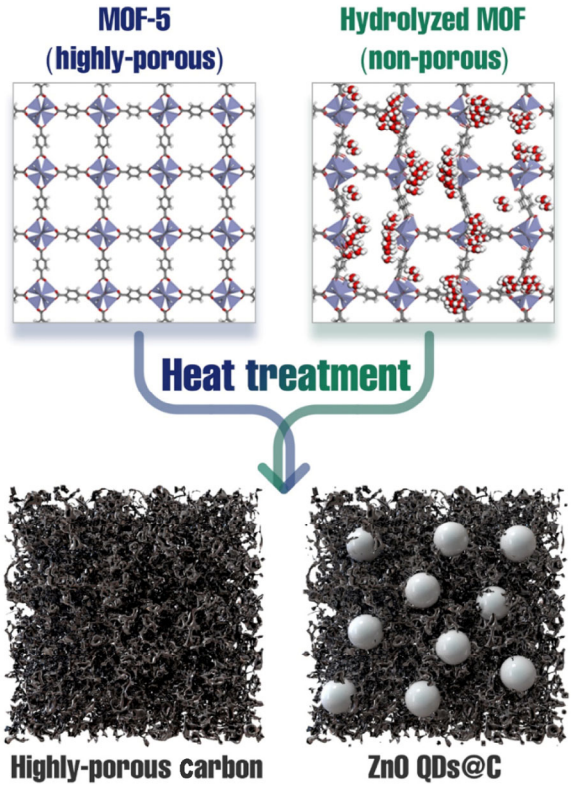

Scheme 1 Schematic illustration of MOF-5 (MOF), hydrolyzed MOF-5 (h-MOF), and the resulting porous MOF-derived materials (MDC, h-MDC, MDC@ZnO, and h-MDC@ZnO) from two different precursors. The regeneration of porosity and the formation of ZnO quantum dots during the thermal process are highlighted. The content of ZnO quantum dots in the product can be tunable by adjusting heat treatment temperature.

potential use as a precursor for the hybridization of MOFs with other nanomaterials.

Herein, the hypothesis of MOF protection against the notorious hydrolysis was revisited and the usefulness of hydrolyzed MOF was re-evaluated for the synthesis of MOF-derived materials. It was revealed that the degraded porosity can be regenerated during the simple thermal treatment in the hydrolyzed MOF sample. The h-MDC@ZnO-rGO was also prepared as a representative for other MOF-derived materials made from water-based synthetic processes. The composite was obtained by mixing water-dispersed GO and MOF followed by a simple thermal treatment at 570 °C. In addition, metal oxide quantum dot (QD) can be controllably formed by adjusting heat treatment temperature. The hydrolyzed-MOF derived carbon enveloped with reduced GO (rGO) and decorated with ZnO QDs (denoted as h-MDC@ZnO-rGO) was assessed as an energy storage material and showed superior electrochemical performance of approximately 500 $mA{\cdot}h{\cdot}g^{-1}$ at a very high *C* rate of 5 C (3,750 $mA{\cdot}g^{-1}$). Ironically, hydrolysis appears to be a new and facile way to prepare MOF-derived materials for future applications, such as energy storage materials.

2 Results and discussion

The schematic illustration in Scheme 1 shows the two different precursors for the porous MOF-derived materials including (1) porous MOF-derived carbons and (2) porous MOF-derived carbons with zinc oxide quantum dots (ZnO QDs). The hydrolyzed MOF (denoted as h-MOF) was compared with the intact MOF-5 (denoted as MOF) to determine if the effect of hydrolysis is nullified during the thermal treatment. The hydrolysis of MOF resulted in the complete loss of porosity due to structural changes compared to the preserved porosity in the intact MOF. On the other hand, the resulting products of h-MOF after the heat treatment (denoted as h-MDC and h-MDC@ZnO; they differed from the existence of ZnO QDs) were similar to the heat treatment results of intact MOF. This suggests that maintenance of the original porosity of MOFs is not essential for the preparation of MOF-derived materials. If the atomic distribution of elements is guaranteed, the degraded porosity might be regenerated during the heat treatment, regardless of how much the change in original MOF structure occurs. This hypothesis has proven to be correct and the atomic distribution of Zn, C, and O is more important than retaining the original porosity in the preparation of MOF-derived materials. In addition, the formation of ZnO QDs can be easily tunable by controlling the heat treatment temperature. Therefore, the utility of h-MOF as valuable as MOF is supported for the preparation of MOF-derived materials.

The following discussions support the hypothesis of the importance of the atomic distribution of elements rather than the original porosity of MOF. The greatly decreased porosity was also recovered up to the level of the intact MOF during thermal treatment. X-ray diffraction (XRD) confirmed the synthesis of MOF, as illustrated by the $(200)_{cubic}$ and $(220)_{cubic}$ peaks showing high crystallinity [34–36]. Physical adsorption of slight traces of water under a dry atmosphere can be removed reversibly from the surface of MOF [30]. To avoid reversible water adsorption and test the hypothesis properly, MOF was deliberately soaked in water from which complete structural degradation of the MOF was expected. To shed light on the hydrolysis mechanism, we prepared several MOF@RH70% samples (denoted as MOF@RH70%-*x*h) by leaving MOF samples under relative humidity of 70%, for controlled time from 1 to 48 h, and compared them with MOF and h-MOF.

As confirmed in Fig. 1(a) and Figs. S1(a)–S1(c) in the Electronic Supplementary Material (ESM), XRD pattern of MOF is completely different from those of h-MOF and MOF@RH70% samples. The peak intensity of (200) at 6.8° and (220) at 9.8° from cubic crystal of MOF were decreased in MOF@RH70%-1 h and the peaks completely disappeared in the following MOF@RH70% samples. In XRD patterns of h-MOF and MOF@RH70% samples, the newly appeared peak at 8.8° indicates the degradation of intact MOF by water molecules [32, 34–36]. To be more specific, it attributes to the appearence of a new phase of $ZnBDC{\cdot}xH_2O$ at 8.8° by periphral Zn–O bond breakdown by hydrolysis and these changes are irreversible unlike physical adsorption of water [32, 37]. Further degradation resulted in formation of zinc terephthalate dihydrates (ZTDH), as characterized by Thirumurugan et al. [38]. The newly appeared peak at 12° indicates the formation of ZTDH in h-MOF. In Fig. S2 in the ESM, the formation of zinc terephthalate dehydrate and $ZnBDC{\cdot}xH_2O$ were also observed in h-MOF@water_3Days as the evidence of hydrolysis. This is similar to the result of h-MOF (Fig. S1(a) in the ESM). This indicates that even short exposure to water can significantly change the structure of MOF. Therefore, the new reflection in h-MOF is assigned to the appearence of a mixture phase of $ZnBDC{\cdot}xH_2O$, terephtahalate dihydrate, and some unknown phases. A computational study also supported that the oxygen atoms in the Zn_4O center in MOF lost its coordination state and was replaced by oxygen atom in water molecules [27].

The evidence of hydrolysis was also found in Fourier transformed infrared (FT-IR) and X-ray photoelectron spectroscopy (XPS) results of the samples in Figs. 1(b)–1(d) and Fig. S1 in the ESM. The highlighted peak at 3,600 cm^{-1} is assigned to O–H stretching from water-absorbed Zn sites. The broad peak from 3,400 to 3,000 cm^{-1} is similarly assigned to O–H stretching as a result of the displacement of oxygen in the BDC linker by water molecule. The inserted water molecule in MOF dissociated and resulted in formation of hydroxyl group dangled on Zn site and carboxylic acid at the linker [31]. The detected carbonyl group in both h-MOF and MOF@RH70% samples supports the decomposition reaction.

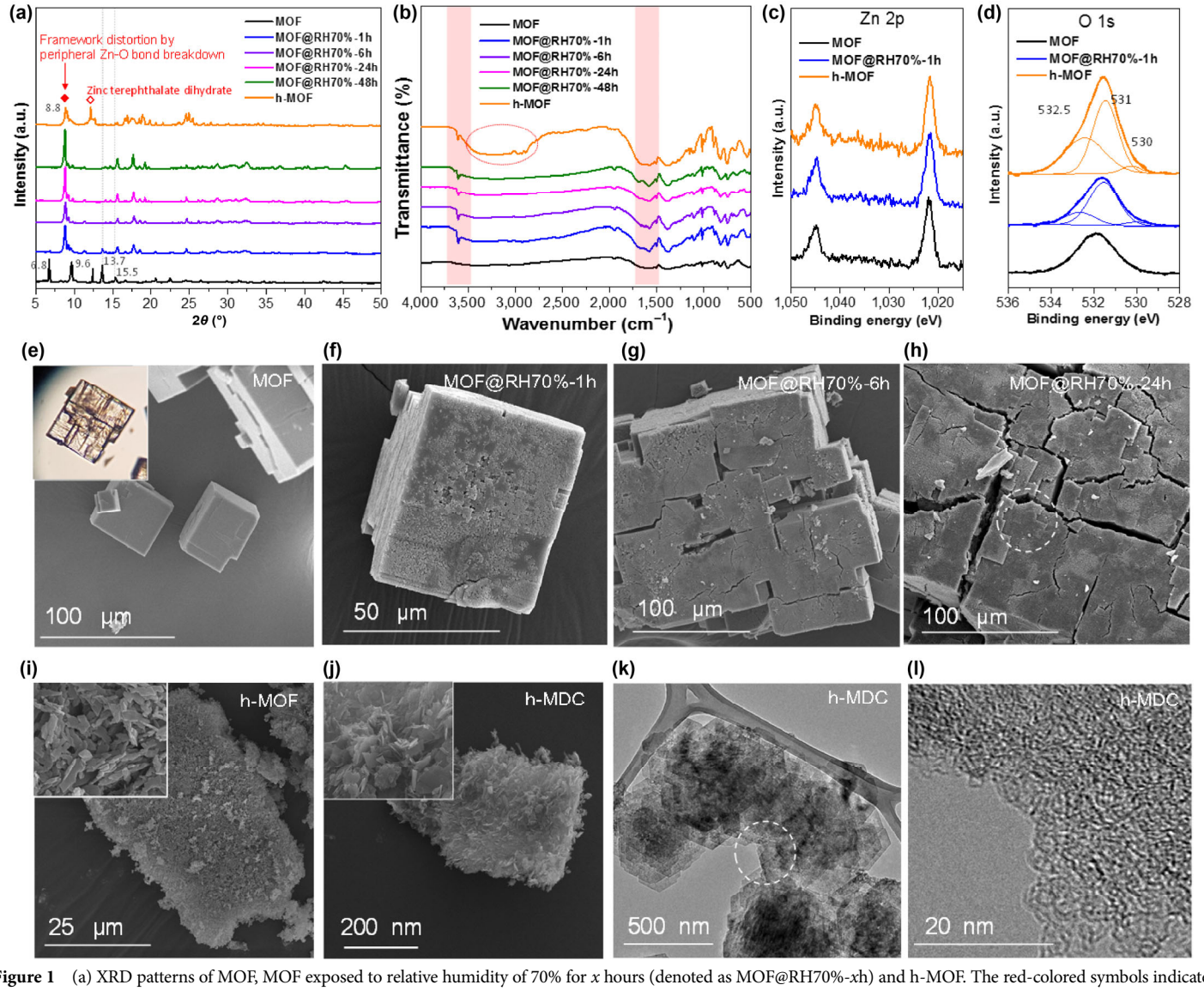

Figure 1 (a) XRD patterns of MOF, MOF exposed to relative humidity of 70% for *x* hours (denoted as MOF@RH70%-*x*h) and h-MOF. The red-colored symbols indicate the decomposition and distortion of framework of MOF by Zn–O bond breakdown and formation of zinc terephthalate dihydrate. (b) FT-IR spectra for the samples and the characteristic changes are highlighted. (c) Zn 2p peaks of MOF, MOF@RH70%-1h, and h-MOF. (d) Deconvoluted O 1s peaks of the samples. SEM images of (e) MOF, (f) MOF@RH70%-1h, (g) MOF@RH70%-6h, (h) MOF@RH70%-24h. (i) h-MOF with magnified surface as inset, and (j) h-MDC with the magnified surface SEM image as inset. TEM images of h-MDC in (k) low resolution and (l) high resolution. The white-colored dashed circle indicate the magnified surface of the sample.

In Fig. S1(d) in the ESM, the XPS spectra were acquired for MOF, MOF@RH70%-1h, and h-MOF. For all the samples, the Zn 2p spectra (Fig. 1(c)) were obtained at 1,022.5 and 1,045.5 eV corresponding to Zn $2p_{3/2}$ and $2p_{1/2}$ components, respectively. The Zn 2p core levels are insensitive to the Zn oxidation state [39]. Therefore, O 1s peak might identify the change of MOF by H_2O exposure. As shown in Fig. 1(d), the carboxylate peak at 531 eV for O^- 1s state and metal hydrooxide at 532.5 eV for O^{2-} 1s state were developed by the exposure of water molecules. These originate from the chemisorbed oxygen species of water on the surface of MOF [39, 40].

The structural changes in h-MOF and MOF@RH70% samples were also visually verified by scanning electron microscopy (SEM) micrographs. In Figs. 1(e)–1(h) and Fig. S3 in the ESM, the surface crack and fragments of MOF were observed by the increase of the exposure time to water molecules. In h-MOF, it seemed that polycrystalline three-dimensional (3D) MOF cubes (Fig. 1(e)) were changed to the accumulation of the two-dimensional (2D) sheet-like fragments (Fig. 1(i)). The increasing trend of the observed 2D sheet-like fragments in the samples supported the decomposition of the original MOF structure by the hydrolysis [34–36, 41]. It is noteworthy that the oxygen content in the sample increased by the exposure to water molecules (Fig. S4 in the ESM), which is indicative of the irreversible reaction between MOF and water molecules. The degradation of cubic crystal of MOF also resulted in the decrease in its dimension from 3D to 2D and decreased specific surface area (SSA) (Fig. S1(e) in the ESM). Interestingly, h-MOF still preserved the atomic distribution of Zn, O, and O despite the size reduction by the distortion and decomposition of MOF structure. The preserved local atomic distribution is confirmed by uniform distribution of elements (C, O, Zn) in the energy-dispersive spectroscopy (EDS) mapping of MOF and h-MOF (Fig. S4 in the ESM).

The atomic distributions of Zn, O, and C in h-MOFs despite the irreversible hydrolysis reactions suggest that h-MOF would be a useful precursor for the hybridization of MOFs with other nanomaterials.

To reevaluate h-MOF as a precursor for MOF-derived materials, both h-MOF and MOF were treated thermally at 900 °C under inert conditions. SEM images (Fig. 1(j) and Fig. S3(a) in the ESM) and transmission electron microscopy (TEM) image (Figs. 1(k) and 1(l)) showed resulting porous MOF and h-MOF derived carbons (denoted as MDC and h-MDC, respectively). Interestingly, the shape of h-MDC maintained the shape of its precursor (h-MOF) the same as

MDC. The heat treatment process turned the two precursors into porous carbons without the change of the precursor's original morphology. The physical difference in h-MDC and MDC is in their size. By comparing Fig. 1(j) and Fig. S3(a) in the ESM, the very small size of h-MDC (~ 1/500 of MDC) was originated from the hydrolysis of MOF. As the water molecules attack and reorientate the elements of MOFs [42], the morphology changed from 3D cubes to fragmentized sheets and debris as shown in Fig. 1. The fragmentized h-MDC and h-MOF might have additional merit in hybridization with other one-dimensional (1D) and 2D materials, such as graphene and GO, compared to the bulk micrometer-sized cubic-like MDC and MOF [43–45].

Although XRD, FT-IR, XPS, TEM, and SEM (Fig. 1 and Figs. S1–S4 in the ESM) confirmed the structural rearrangement of h-MOF, it is interesting that the thermal treatment of h-MOF and MOF resulted in similar porous nanocarbon in terms of porosity. As shown in Fig. S5(a) in the ESM, the XRD patterns of the h-MDC and MDC showed typical patterns of porous carbon [46]. In addition, the I_D/I_G ratio between the intensity of the D-band peak (1,320 cm^{-1}) and that of the G-band peak (1,590 cm^{-1}) using Raman spectroscopy supports the existent of amorphous carbon and sp^2 carbon in both MDC and h-MDC. The calculated I_D/I_G ratio of MDC and h-MDC is 0.98 and 1.02, respectively (Fig. 2(a)). The amorphous carbon in the MDC and h-MDC had a rough surface, as observed in the SEM and TEM images (Fig. 1(j) and Fig. S3(a) in the ESM).

The SSA of the resulting MDC and h-MDC were quantified, and compared with that of MOF and h-MOF using the nitrogen adsorption isotherm (Figs. 2(b) and 2(c)) at 77 K. Hydrolysis deteriorated the pore structure of MOF entirely, as supported by the complete loss of SSA in h-MOF (Fig. 2(b)). The SSA of MOF was calculated to be 1,100 $m^2 \cdot g^{-1}$, while the value of h-MOF was less than 1% of MOF, 6 $m^2 \cdot g^{-1}$. The dramatic increase in SSA after thermal treatment suggests that the degenerated pores of h-MOF was restored during the heat treatment process. The SSA of MDC was calculated to be 1,650 $m^2 \cdot g^{-1}$, corresponding to a 150% increase and that of h-MDC was calculated to be 1,380 $m^2 \cdot g^{-1}$. Although the value of h-MDC was slightly lower than that of MDC, the increase in SSA during the heat treatment was as high as 23,000%. This extraordinary regeneration in the SSA of h-MOF suggests that the atomically localized state of the elements (Zn, O, and C) does matter in preparing MOF-derived materials despite the changes in its crystal structure due to hydrolysis. It should be noted that there was no ZnO particles in the h-MDC and MDC, as characterized by Raman, XRD and EDAX analysis (Figs. 2(a), 2(d) and Fig. S6 in the ESM). Therefore, the high SSA values of MDC and h-MDC are reasonable values and in good agreement with Ref. [47]. For the preparation of porous MOF-derived carbon, MOF and h-MOF underwent high temperature up to 900 °C. During the thermal treatment of intact MOF, the ZnO was firstly formed due to the decomposition of the MOF framework at approximately 500 °C. At the higher temperature, the formed ZnO was reduced to Zn metal and carbonization process underwent: ZnO (s) + C (s) → Zn + CO_x. Finally, Zn metal (boiling point 908 °C) vaporized away, leaving the porous carbons only [48, 49]. This mechanism is so-called the self-vanishing porogen mechanism [47]. In h-MOF, the ZnBDC and ZTDH also decomposed to ZnO, which is similar to the case of Ref. [50]. The subsequent carbonization and Zn metal vaporization similarly occurs just like the case of MOF. Therefore, the morphological difference in the precursors and the water-induced rearrangement and distortion of bonding in MOF did not appear to be critical in producing MOF-derived materials. This is presumably related to the mechanism of MDC synthesis. The Zn in the MOF induces the decomposition of carbon and a reaction with oxygen in both MOF and h-MOF.

By controlling the heat treatment temperature, MOF can be turned into ZnO-embedded MDC in the accessible pores of the amorphous carbon [51]. In the previous study, ZnO-embedded porous carbon was prepared using this phenomenon [52]. Same as intact MOF, the atomically distributed elements including Zn atoms were maintained although the crystal structure was changed as observed in Fig. 1(a). Therefore, the heat treated products of h-MOF and MOF could be similar to each other because atomically distributed Zn atom can play critical roles as self-vanishing template for porous

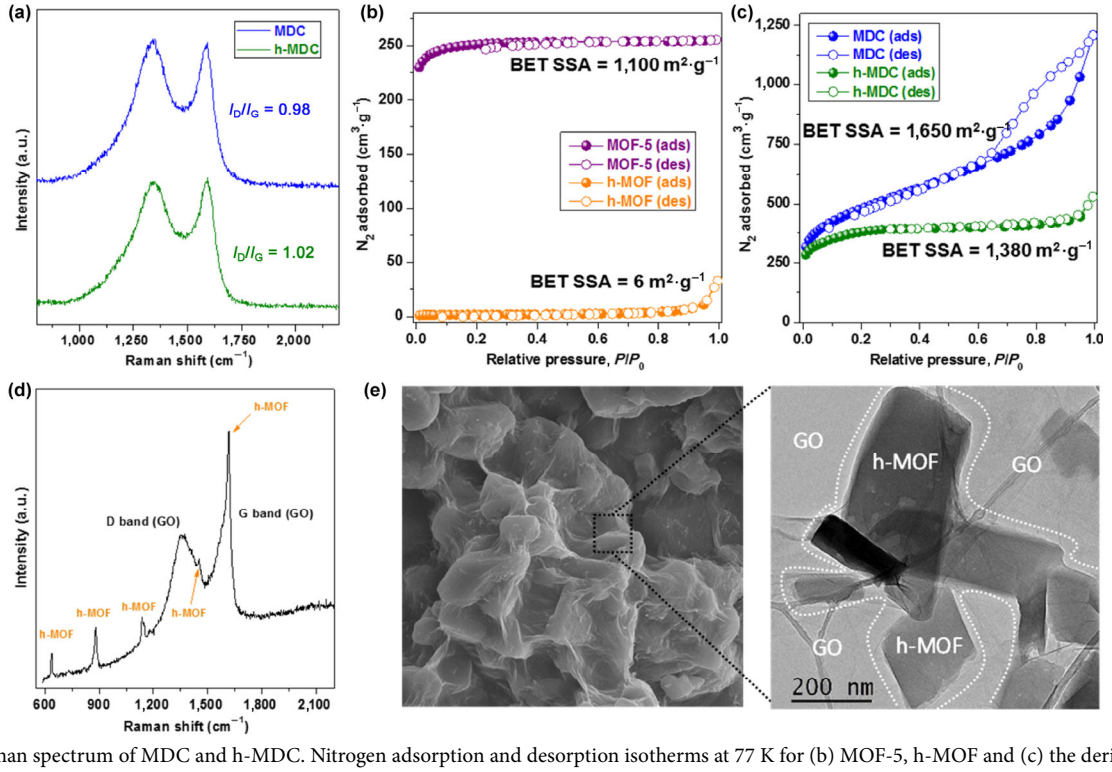

Figure 2 (a) Raman spectrum of MDC and h-MDC. Nitrogen adsorption and desorption isotherms at 77 K for (b) MOF-5, h-MOF and (c) the derived porous MDC and h-MDC (note that there are no ZnO QDs in MDC and h-MDC). (d) Raman spectrum of the hybrid h-MOF-GO composite. (e) SEM (left side) and TEM (right side) images of the hybrid composite.

carbon and ZnO QDs formation during the heat treatment. The importance of the atomically dispersed metal site is recently discussed in Ref. [53]. Therefore, preserving the original structure of MOF is not essential only if the atomic distribution of elements are guaranteed. This implies that the distorted and even decomposed MOF by hydrolysis can be used as a precursor for MOF-derived materials. Therefore, h-MOF can be a good candidate as a precursor for a range of MOF-derived materials and fabricate using water-based process.

The pore regeneration process enables the introduction of a water-based process for the fabrication of the various nanocomposites, as shown by the results of the h-MDC@ZnO-rGO hybrid composite. A combination with graphene, having versatility for enhancing the mechanical and electrical properties of nanocomposites, can be a good way of producing advanced nanocomposites for future applications [54–56]. A previously study reported ZnO QDs embedded porous carbon using MOF, which displayed outstanding electrochemical performance [52]. On the other hand, it has an inherent limitation in the electrical property due to the less-conductive amorphous carbon. In addition, conversion reactions based lithium storage including ZnO suffered from the significant volume change during cycling.

The sandwich-like structure with graphene can relieve the pulverization of active materials by acting as structural support [57, 58]. For that reason, the assembly of graphene and MOF aims to improve the results in previous studies. A composite of the two was produced by simple mixing of a GO solution with an h-MOF solution with the post thermal treatment. The assembly of h-MOF and GO nanocomposite is self-driven by the electrostatic interactions between the negatively charged GO (−40.05 mV) and positively charged h-MOF (3.96 mV). During the heat treatment of the h-MOF-GO mixture, the degraded porosity due to water molecules in h-MOF can be regenerated and the electrical properties of the composite can be improved simultaneously by reducing GO to rGO. The hybrid solution of h-MOF and GO can be prepared simply as a freestanding film, as shown in Fig. S5(b) in the ESM. The Raman spectrum of the h-MOF-GO sample (Fig. 2(d)) also confirmed the coexistence of h-MOF and GO [42].

SEM and TEM showed the assembly of h-MOF-GO composites (Fig. 2(e)). The 200–400 nm-sized h-MOF particles were anchored intimately to the surface of GO and wrapped with GO. The low-resolution SEM image showed uniform sandwiched MOF particles between the GO sheets (Fig. S7 in the ESM). The heat treatment turned h-MOF-GO to h-MDC@ZnO-rGO. Interestingly, h-MDC@ZnO-rGO still maintained the sandwich-like hybrid structure and the atomic distribution of elements (Zn, O, and C) as supported by EDS mapping (Fig. S8 in the ESM).

This sandwich hybrid structure, in which electrochemical active materials were layered between electrically conductive graphene sheets, tends to deliver superior electrochemical performance [59, 60]. The sandwich hybrid structure with graphene is beneficial to the conversion of reaction-based lithium storage material including ZnO. Because the hybrid structure is able to hold the volume change during cycling by providing structural support to enhance the mechanical integrity of the electrode [57, 58].

The heat treatment in an inert atmosphere (1) reduces GO to rGO, (2) modifies h-MOF to ZnO QDs-embedded amorphous carbon, and (3) regenerates the porosity of the MOF while reserving the sandwich hybrid structure. Retention of ZnO QDs is a key to maximize the electrochemical performance of ZnO-based conversion reactions during cycling [57, 58]. To maintain the nano size of QDs, the heat treatment temperature should be carefully controlled because Ostwald ripening of ZnO QDs easily occurs [61]. In Fig. S9 in the ESM, the characteristic peaks of ZnO QDs were detected above 560 °C. On the other hand, ZnO QDs appeared to be overgrown at high temperatures (580 °C) by Ostwald ripening [61], which is unfavorable for the integrity of the hybrid structure. The structural integrity appeared to be best reserved at 570 °C during the process, as observed in SEM images of the h-MDC@ZnO-rGO composite (Figs. 3(a), 3(b), and Fig. S10 in the ESM). Therefore, the ZnO QD embedded h-MDC (h-MDC@ZnO) was tightly sandwiched with rGOs, reserving the morphology to the h-MOF-GO sample. TEM and selected-area electron diffraction (SAED) (Fig. 3(c) inset) also showed that ZnO QDs surrounded by amorphous carbon are distributed uniformly over the rGO surface. SAED of the sample indicated a hexagonal wurtzite crystal structure of ZnO, suggesting that the resulting carbon is amorphous. This was also confirmed by high-resolution TEM, as shown in Figs. S11 and S12 in the ESM.

The crystalline size of the ZnO quantum dots can be calculated

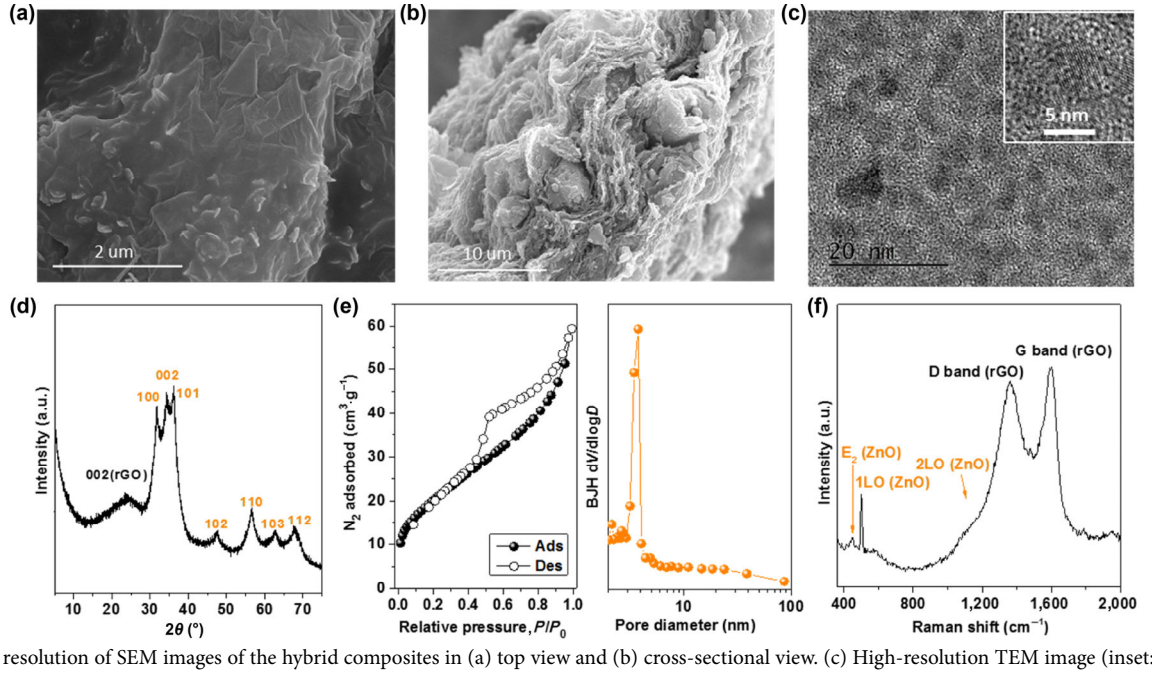

Figure 3 High resolution of SEM images of the hybrid composites in (a) top view and (b) cross-sectional view. (c) High-resolution TEM image (inset: enlarged view) of the h-MDC@ZnO-rGO sample. (d) XRD patterns of the h-MDC@ZnO-rGO sample. (e) Nitrogen adsorption and desorption isotherms and pore size distribution of the h-MDC@ZnO-rGO. (f) Raman spectrum of the h-MDC@ZnO-rGO sample.

by using Scherrer's equation and the full width at half maximum can be obtained from fitting the ZnO peaks of (110), (002), and (101). From the curve-fitted diffraction parameters (Fig. S13 in the ESM), the calculated crystalline size of the h-MDC@ZnO-rGO is about 3.97 nm. This is in good agreement with that from TEM image of ZnO QDs in the sample.

The ZnO QDs with a mean particle size of 4 nm were dispersed uniformly and wrapped intimately with an amorphous carbon matrix. The uniform distribution of elements was well maintained even after the thermal treatment (Figs. S11 and S12 in the ESM). The reaction temperature affects the size and morphology of the resulting ZnO significantly [61]. Considering that ZnO can be aggregated easily during thermal treatment, the sandwich structure of h-MDC-rGO inhibits the aggregation of ZnO and a uniform distribution of ZnO QDs (4 nm) can be achieved.

XRD showed the characteristic (002) peak of rGO and MDC. The existence of ZnO peaks were detected between 30° to 40° in XRD patterns and observed between 400 and 600 cm^{-1} in Raman spectra (indexed as a yellow color, Figs. 3(d) and 3(f)). The pore size distribution based on the Barrett–Joyner–Halenda (BJH) equation showed a micropososity of the product centered at 2 nm and uniformly distributed mesopores (Fig. 3(e)). The micropores might have originated from the amorphous carbon on the outer shells of ZnO, whereas the others might be due to the gap between rGO and ZnO-embedded amorphous carbon particles. Such well-developed porosity was attributed to the uniformly delocalized elements in the precursor (h-MOF) and the sandwich hybrid structure with GO, which was driven by electrostatic self-assembly. This well-developed porosity can be extra ion storage sites and an effective lithium ion diffusion pathway for energy storage applications [62]. Considering the negligible porosity in rGO films, the hybridization of h-MDC@ZnO and rGO has a positive impact on developing porosity, thereby possessing ion accessibility. In addition, the coexistence of ZnO QDs and porous carbon increased the electrochemical performance [52].

The function-regenerated h-MDC@ZnO-rGO composites were fabricated and assessed as an electrode material for lithium ion batteries. As discussed previously, the sandwiched hybrid structure of the electrochemically active ZnO QDs and superior electrical conductive graphene layer in the h-MDC@ZnO-rGO composite could lead to the following merits. (1) Mesopores in-between the graphene sheets act as a diffusion pathway to the ZnO QDs (redox sites) [63]. (2) Intimately ZnO-anchored graphene layers can guarantee a rapid electron transport pathway to the redox sites [63]. (3) 2D sheets of graphene layers can also act as an elastic buffer layer to accommodate the expansion of ZnO QDs during the lithiation and keep the mechanical integrity of the electrode [64].

Before discussing the lithium storage performance of h-MDC@ZnO-rGO, the lithium storage mechanism is investigated using cyclic voltammograms (CVs). In the initial and following scan, lithium storage reaction is based on the following two reactions: $ZnO + 2Li^+ + 2e^- \rightarrow Zn + Li_2O$ and $Zn + Li^+ + e^- \rightarrow LiZn$. In the CV analysis (Fig. 4(a)), the broad shoulder around ~ 1.0 V and the strong peak at ~ 0.1 V supported the reduction of ZnO to Zn and the formation of Li–Zn alloy, respectively, which is in good agreement with the previous study with ZnO nanoparticles [65]. In the initial scan of h-MDC@ZnO, the characteristic peak was embed with the peak related to the formation of solid electrolyte interface [66].

However, the subsequent scan revealed the peak related to the reduction of ZnO QDs. In the anodic scan, the ZnOs were formed during the delithiation. The broad shoulder below 0.5 V assigned to the multi-step delithiation of LiZn through $LiZn \rightarrow Li_2Zn_3 \rightarrow LiZn_2 \rightarrow Li_2Zn_5 \rightarrow Zn$ [67, 68]. Compared to the h-MDC@ZnO sample, the redox peak shift of ZnO from 1.3 to 1.1 V was observed, implying the improved reversibility of ZnO formation in h-MDC@ZnO-rGO.

This result can be attributed to the sandwich-like structure with rGO and is also consistent with the galvanostatic test results. The electromotive force of the reaction ($ZnO + 2Li^+ + 2e^- \rightarrow Zn + Li_2O$) can be calculated from the standard Gibbs free energies of formation of ZnO and Li_2O, which is ~1.26 V vs. Li^+/Li, and the respective capacity is 978 $mA{\cdot}h{\cdot}g^{-1}$ [69].

As shown in Fig. S15 in the ESM, the charge/discharge curves exhibited the typical profile of a ZnO-carbon electrode which was in good agreement with CV result (Fig. 4(a)). The discharge capacity of the sample exceeded that of the ZnO-based anode materials [70] and was even similar MDC@ZnO QDs to that of a previous study [52]. A part of the extra capacities comes from carbon black (~ 107 $mA{\cdot}h{\cdot}g^{-1}$) and the remainder originates from the adsorption of Li to the micropores of 2 nm [62]. Because the rough surface of h-MDC@ZnO, which results from the micropores, can also serve as a reservoir for the electrolyte, the access of Li^+ to the redox sites is facilitated, compared to that through the relatively-smooth surface of MDC. Irreversible capacity was measured as 559 $mA{\cdot}h{\cdot}g^{-1}$ at the initial cycle. This is 34.8% loss from the total discharge capacity. The initial capacity loss originated mainly from the formation of a solid-electrolyte interphase (SEI) layer on the electrode surface [71]. The capacity was saturated from the subsequent cycles. On the other hand, the initial loss in the h-MDC@ZnO-rGO electrode was lower than that in recent reports on the porous MDC@ZnO-based anode materials, approximately 50% of the loss [52].

Compared to the amorphous carbon, the graphene layers in the sandwich structure provide a better electronic conductive matrix and more stable carbon. The graphene layers helped improve the irreversible continuous interphase formation [73]. As confirmed by EIS (Fig. 4(f)), the h-MDC@ZnO-rGO electrode showed substantially lower resistance than the h-MDC@ZnO electrode. This suggests that the graphene layers play a synergistic role on improving the initial capacity loss.

The h-MDC@ZnO-rGO electrode shows stable cyclability under a current density of 75 $mA{\cdot}g^{-1}$, as shown in Fig. 4(c). The long-term stability might come from the amorphous carbon layer around the ZnO QDs, which makes a contribution to buffering volume expansion of ZnO during cycling [73]. Furthermore, even at a high current density of 1,500 $mA{\cdot}g^{-1}$, the material showed a reversible capacity of 620 $mA{\cdot}h{\cdot}g^{-1}$ for 200 cycles, as shown in Fig. 4(d). The sandwiched architecture retained the integrity of the ZnO QDs and graphene, hence the outstanding cycle-life performance.

The rate capability was tested under the various charge/discharge current densities of 75, 150, 375, 750, 1,500, and 3,750 $mA{\cdot}g^{-1}$, as shown in Fig. 4(e). The resulting discharge capacities were 1,118, 997, 842, 728, 620, and 497 $mA{\cdot}h{\cdot}g^{-1}$, respectively. Compared to the 30.7% capacity retention of the initial capacity of the ZnO QDs-embedded amorphous carbon electrode (Fig. S16 in the ESM), the h-MDC@ZnO-rGO electrode maintained 44.5% of the initial capacity. To give an insight on h-MDC@ZnO, the capacities of h-MDC@ZnO and MDC@ZnO (570 °C) at various current densities were measured (Fig. S20 in the ESM). The capacities of them were similar at low current density of 75 and 150 $mA{\cdot}g^{-1}$. At 75 $mA{\cdot}g^{-1}$, h-MDC@ZnO and MDC@ZnO (570 °C) exhibited 869 and 854 $mA{\cdot}h{\cdot}g^{-1}$, respectively. This is in the range of the theoretical capacity of ZnO QDs with amorphous carbons. However, the rate capability was better in MDC@ZnO (570 °C). The capacities of h-MDC@ZnO and MDC@ZnO (570 °C) at 1,500 $mA{\cdot}g^{-1}$ were 116 and 427 $mA{\cdot}h{\cdot}g^{-1}$, respectively. The poor rate capability in h-MDC@ZnO might be attributed to the relatively bigger size (4 nm) of ZnO QDs than MDC@ZnO (2 nm). In addition, relatively more irregular surface of h-MDC@ZnO can hamper the diffusion of lithium ion at high rate. However, this trend becomes the opposite in the composite electrodes with rGO.

In Fig. 4(e), the electrochemical result of h-MDC@ZnO showed relatively poor rate capability compared to h-MDC@ZnO-rGO sample. This indirectly supports the synergistic effect from the sandwich-like structure with rGO. To be more specific, ZnO QDs suffered from the volume change during cycling. During lithiation,

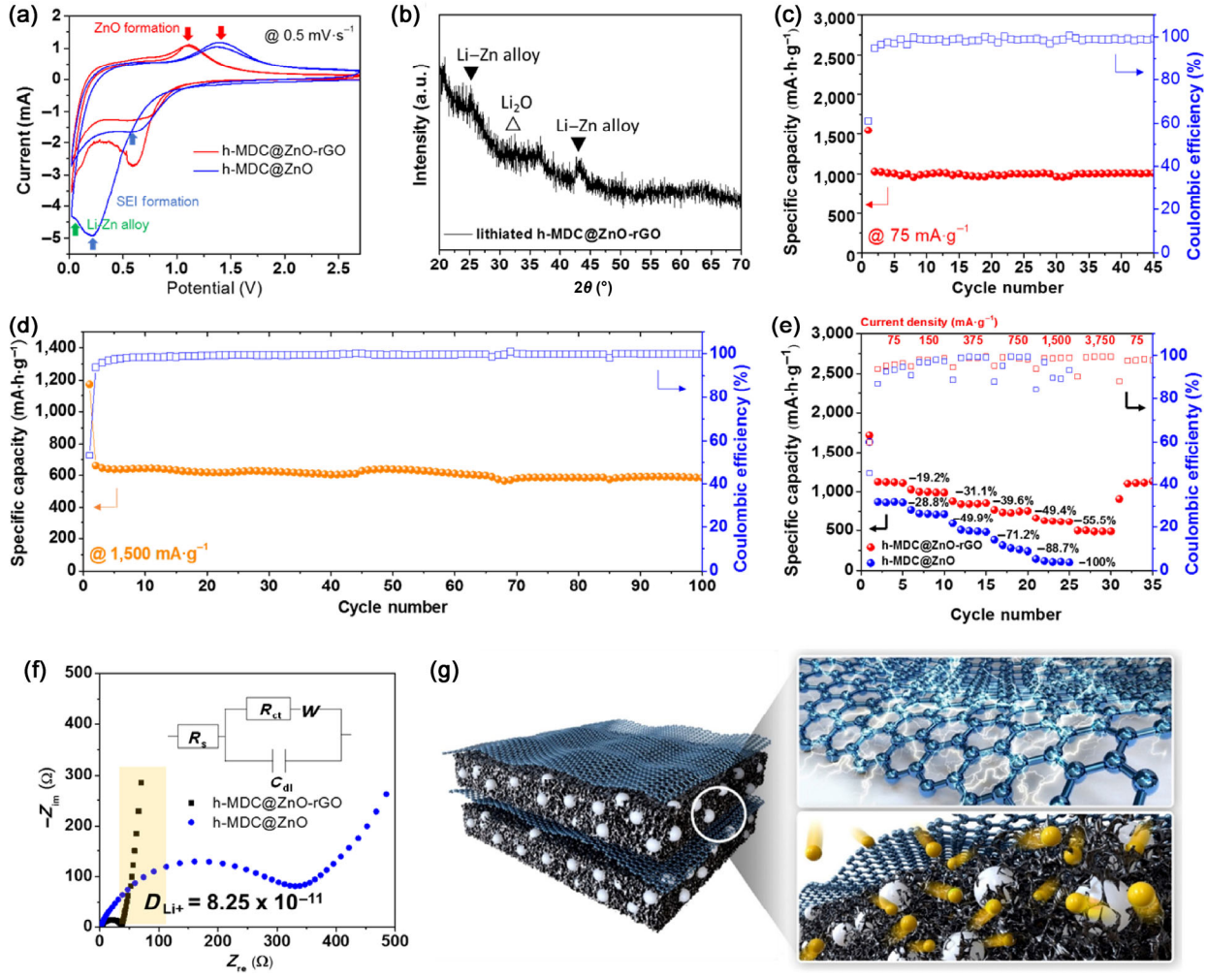

Figure 4 (a) Cyclic voltammograms of h-MDC@ZnO-rGO and h-MDC@ZnO at 0.5 mV·s^{-1}. (b) XRD patterns of lithiated h-MDC@ZnO-rGO electrode. (c) Specific discharge capacities and corresponding Coulombic efficiency of h-MDC@ZnO-rGO composite at the low current density of 75 mA·g^{-1}. (d) Long-term cycle stability at the high current density of 1,500 mA·g^{-1}. (e) Specific discharge capacities and corresponding Coulombic efficiencies of h-MDC@ZnO-rGO and h-MDC@ZnO at various current densities from 75 to 3,750 mA·g^{-1}. Specific capacity loss rates at varying current densities are given in black-colored numbers. (f) Nyquist plots for the hybrid h-MDC@ZnO-rGO composite with the diffusion coefficient of lithium ions and compared to the h-MDC@ZnO electrode. (g) Schematic illustration of the synergistic effect of the hybrid composite from the rapid electron transport and structure support by rGO and the fast ion accessibility through porous h-MDC@ZnO.

ZnO QDs are reduced to Zn, followed by Li–Zn alloy formation [61, 62, 67]. As supported by CVs in Fig. 4(a), the hybridization with reduced graphene showing sandwich-like structure enhanced the reversibility. It can be concluded that the enhanced rate capability of h-MDC@ZnO-rGO is attributed to (1) rGO that acts as a structural support, retaining the mechanical integrity and (2) enhanced electron transfer from conductive graphene layers to ZnO QDs [67, 68, 74] (Figs. 4(d) and 4(e)). To access the utility of h-MOF further, MDC@ZnO-rGO were prepared for the comparison with h-MDC@ZnO-rGO. To prepare the MDC@ZnO sample, the intact MOF was synthesized and carbonized into MDC@ZnO in sequence. Then, the product was uniformly mixed with graphene oxide solution. The vacuum filtered MDC@ZnO-GO samples were thermally treated to reduce the graphene oxide. During the thermal treatment, the physical delamination between MDC@ZnO and rGO might occur due to the lacked interaction between them. Therefore, the better electrochemical performance of h-MDC@ZnO-rGO can be explained by the intimate interaction between redox active ZnO particles and graphene layers unlike the case of MDC@ZnO-rGO (Fig. S17 in the ESM). The intimate contact in h-MDC@ZnO-rGO is due to the electrostatically induced self-assembly in h-MOF@GO as confirmed by zeta potential. Therefore, h-MOF@GO can be easily transformed into the sandwich-like structure of graphene layer and ZnO@C as illustrated in Fig. 4(g). In addition, the synthetic process for h-MDC@ZnO-rGO is much simpler than MDC@ZnO-rGO.

It should be noted that the capacity is the total sum of the contribution from ZnO QDs and that from the amorphous carbon and rGO. Therefore, the normalized capacity of h-MDC@ZnO-rGO was 746 mA·h·g^{-1} based on the following calculation: 981 (ZnO) × 0.51 + 501 (carbons; Fig. S18 in the ESM) × 0.49 = 746 mA·h·g^{-1}. The capacity of amorphous carbon and rGO after removal of ZnO QDs is displayed in Fig. S19 in the ESM. The synergistic effect from the interfacial regime of ZnO and rGO might occur below 0.2 V. Considering that the discharged product L_2O can act as an ionic conductor while rGO and Zn play a role of electron conductor, the so-called "Job-sharing mechanism" is able to happen at the interfacial regime. The excess capacity in h-MDC@ZnO-rGO can be explained by this mechanism [75–77].

The electrochemical impedance spectra of the electrodes were obtained to gain insight into the synergistic effect of h-MDC@ZnO-rGO composite. As shown in Fig. 4(f), the charge transfer resistance and the calculated diffusion coefficients were enhanced considerably in the composites. The diffusion coefficient of Li^+ in the h-MDC@ZnO-rGO electrode was 8.25 × 10^{-11} cm^2·s^{-1}, which is a much higher value than that of the commercial graphite electrode (2.45 × 10^{-12} cm^2·s^{-1}) [78]. The improved ionic and electronic transport via regenerated pores and enhanced electronic pathway through rGO can play a synergistic role, as shown schematically in Fig. 4(g).

3 Conclusions

By revisiting h-MOF, we have shown that the preparation of various MOF-derived materials including MDC, MDC@ZnO, and their composites with rGO is successfully done by the simple and practical water-based process. The properties of h-MOF-derived functional materials were almost equivalent to that of MOF-derived materials. We find that the function degeneration due to hydrolysis can be overcome by the heat treatment in contrast to the long-held axiom that the structural change in MOF from hydrolysis is irreversible, limiting its usability. With the demonstration of the function-regenerated h-MDC@ZnO-rGO composites as an anode material for lithium-ion batteries, the versatility of h-MOF is highlighted. The h-MDC@ZnO-rGO exhibited superior lithium storage performance, showing reversible capacity of 620 mA·h·g^{-1}, even at a current density of 1,500 mA·g^{-1}. This finding will expand the realm of MOF further to the unprecedented applications where the high humidity is expected.

4 Experimental section

4.1 Reagents and chemicals

Graphene oxide solution (GO-A400, Grapheneall, Korea), zinc nitrate tetrahydrate (Merck), terephthalic acid (Aldrich), and N,N-dimethylformamide (DMF; Daejung, Republic of Korea) were used without additional purification or modification.

4.2 Synthesis of MOF

Zinc nitrate tetrahydrate (0.784 g, 3 mmol) and terephthalic acid (0.166 g, 1 mmol) were dissolved in 30 mL DMF in a 40 mL vial. The solution was heated in an oven at 105 °C for 24 h to yield crystals of MOF. The reaction vial was removed from the oven and cooled to room temperature for 1 h. The resulting cubic crystals of MOF were washed repeatedly with DMF and soaked in anhydrous chloroform for 24 h, followed by filtration. The filtered cubic crystals were vacuum-dried at 150 °C for 24 h.

4.3 Preparation of hydrolyzed MOF (MOF@RH70% samples)

The MOF@RH70% samples were prepared by resting MOF in the chamber of the relative humidity of 70% for controlled time from 1 to 48 h.

4.4 Preparation of hydrolyzed MOF

The prepared MOF were soaked in 30 mL of deionized (DI) water in a vial. The vial was stirred for 2 h and sonicated for 1 h. Subsequently, the solution was filtered and dried at 60 °C for 6 h under vacuum conditions. In addition, h-MOF@water_3Days sample was prepared by soaking MOF in DI water for three days and subsequent filtration and drying.

4.5 Preparation of MDC, hydrolyzed MDC (h-MDC), h-MDC@ZnO, and MDC@ZnO (570 °C)

The prepared MOF and h-MOF in crucibles were transferred to a tube furnace and pyrolyzed at 900 °C (under nitrogen atmosphere) at a heating rate of 5 °C·min^{-1} and held at that temperature for 3 h. The materials were cooled naturally to room temperature. The prepared h-MOF and intact MOF were positioned in the crucibles, separately. They were treated thermally up to 570 °C at a heating rate of 10 °C·min^{-1} under a nitrogen atmosphere. The materials were then cooled to room temperature.

4.6 Characterization

Field emission scanning electron microscopy (FE-SEM, S-4300SE) and TEM (JEM-2100F) equipped with EDS were used to analyze the morphology and chemical composition. Multi-purpose X-ray diffraction (PXRD, D8 Advance, Bruker) was carried out in reflection mode using Ni-filtered CuKα radiation ($\lambda \approx 0.154184$ nm). The powdered samples were scanned from 5° to 80° 2θ at a scan speed of 2°·s^{-1}. The chemical properties of the prepared samples were investigated by XPS (AXIS-His, KRATOS). FT-IR spectra of the samples were recorded with a Thermo Scientific NicoletTM iS10 spectrometer to obtain additional information about the change of MOF by the exposure to moisture. Nitrogen adsorption isotherms at liquid nitrogen temperature (77 K) were measured using a Micromeritics ASAP 2020 static volumetric gas adsorption instrument. All gas sorption isotherms were obtained using ultrahigh purity grade gas (99.999%). Prior to gas sorption analysis, the samples (0.1–0.2 g) in the chamber were placed under a vacuum of 10^{-5} Torr with heating at 150 °C for 24 h. Raman spectroscopy was conducted using a RAMAN plus confocal laser Raman microscope (Nanophoton) with a 532 nm laser to identify the surface physicochemical structure of the products. The zeta-potentials were measured using a zeta-potential analyzer (Otsuka). The content of ZnO in the samples was calculated based on thermogravimetric analysis (TGA; SDT-Q600, TA Instruments) from 30 to 1,000 °C at a rate of 10 °C·min^{-1} in 100 mL·min^{-1} of air flow.

4.7 Preparation of h-MOF@GO, h-MDC@ZnO-rGO, and MDC@ZnO-rGO composites

To prepare the h-MOF-GO composites, the as-prepared MOF were soaked in DI water (8.3 mL) in a vial. After blending with 1.7 mL of a graphene oxide solution (GO, 6 mg·mL^{-1}), the mixture was stirred for 12 h, followed by vacuum filtration and vacuum drying at 40 °C for 6 h. For the h-MDC-rGO composites, the prepared h-MOF@GO composites were positioned in the crucibles and treated thermally up to 570 °C at a heating rate of 10 °C·min^{-1} to pyrolyze the h-MOF@GO composite under a nitrogen atmosphere. The materials were then cooled to room temperature. For the MDC-rGO composites, the as-prepared MOF were treated thermally up to 570 °C at a heating rate of 10 °C·min^{-1} to pyrolyze the h-MOF@GO composite under a nitrogen atmosphere. Then, the product was uniformly mixed with graphene oxide solution. The vacuum filtered MDC@ZnO-GO samples were thermally treated at 250 °C for 1 h to reduce the graphene oxide (a heating rate of 10 °C·min^{-1}). The h-MDC-rGO was prepared by soaking in 10 M HCl for 12 h to remove ZnO QDs from h-MDC@ZnO-rGO.

4.8 Electrochemical experiments

The electrode was prepared using the doctor blade coating method with a combination of polyvinylidene fluoride (20 wt.%), carbon black (20 wt.%), and the active material (60 wt.%). The prepared slurry were vacuum-dried and fabricated into a 2032 coin-type half-cell. The average areal loading of electrode is approximately 2 mg·cm^{-2}. The electrochemical tests were carried out using a battery cycler (WBCS3000, WonATech). The galvanostatic charge/discharge tests were performed between 0.02 and 3.0 V and the cyclic voltammetry was conducted between 0.02 and 2.7 V. The potentials were referenced to the Li/Li$^+$ electrode potential. The rate capability was examined at various current densities from 75 to 3,750 mA·g^{-1}. The electrochemical impedance spectra were measured using a potentiostat (ZIVE SP2, WonATech) at the open-circuit voltage with an AC amplitude at 5 mV from the 10 mHz to 100 kHz range.

Acknowledgements

This work was supported by Inha University Research Grant.

Electronic Supplementary Material: Supplementary material (further details of the prepared samples, XRD, XPS, N_2 adsorbed

isotherms, SEM and TEM analysis) is available in the online version of this article at https://doi.org/10.1007/s12274-019-2459-8.

References

[1] Davis, M. E. Ordered porous materials for emerging applications. *Nature* **2002**, *417*, 813–821.

[2] Kitagawa, S. Future porous materials. *Acc. Chem. Res.* **2017**, *50*, 514–516.

[3] Lee, K. J.; Lee, J. H.; Jeoung, S.; Moon, H. R. Transformation of metal–organic frameworks/coordination polymers into functional nanostructured materials: Experimental approaches based on mechanistic insights. *Acc. Chem. Res.* **2017**, *50*, 2684–2692.

[4] Liu, C.; Li, F.; Ma, L. P.; Cheng, H. M. Advanced materials for energy storage. *Adv. Mater.* **2010**, *22*, E28–E62.

[5] Chen, K.; Sun, Z. H; Fang, R. P; Shi, Y.; Cheng, H. M.; Li, F. Metal-organic frameworks (MOFs)-derived nitrogen-doped porous carbon anchored on graphene with multifunctional effects for lithium-sulfur batteries. *Adv. Funct. Mater.* **2018**, *28*, 1707592.

[6] Krause, S.; Bon, V.; Senkovska, I.; Többens, D. M.; Wallacher, D.; Pillai, R. S.; Maurin, G.; Kaskel, S. The effect of crystallite size on pressure amplification in switchable porous solids. *Nat. Commun.* **2018**, *9*, 1573.

[7] Zheng, F. C.; Yang, Y.; Chen, Q. W. High lithium anodic performance of highly nitrogen-doped porous carbon prepared from a metal-organic framework. *Nat. Commun.* **2014**, *5*, 5261.

[8] Jiang, H. L.; Liu, B.; Akita, T.; Haruta, M.; Sakurai, H.; Xu, Q. Au@ZIF-8: CO oxidation over gold nanoparticles deposited to metal-organic framework. *J. Am. Chem. Soc.* **2009**, *131*, 11302–11303.

[9] Liu, B.; Shioyama, H.; Jiang, H. L.; Zhang, X. B.; Xu, Q. Metal–organic framework (MOF) as a template for syntheses of nanoporous carbons as electrode materials for supercapacitor. *Carbon* **2010**, *48*, 456–463.

[10] Kim, T. K.; Lee, K. J.; Cheon, J. Y.; Lee, J. H.; Joo, S. H.; Moon, H. R. Nanoporous metal oxides with tunable and nanocrystalline frameworks via conversion of metal–organic frameworks. *J. Am. Chem. Soc.* **2013**, *135*, 8940–8946.

[11] Zhou, H. C. J.; Kitagawa, S. Metal–organic frameworks (MOFs). *Chem. Soc. Rev.* **2014**, *43*, 5415–5418.

[12] Zheng, H. Q.; Zhang, Y. N.; Liu, L. F.; Wan, W.; Guo, P.; Nyström, A. M.; Zou, X. D. One-pot synthesis of metal–organic frameworks with encapsulated target molecules and their applications for controlled drug delivery. *J. Am. Chem. Soc.* **2016**, *138*, 962–968.

[13] Chen, Y. Z.; Zhang, R.; Jiao, L.; Jiang, H. L. Metal-organic framework-derived porous materials for catalysis. *Coord. Chem. Rev.* **2018**, 362, 1–23.

[14] Jiao, L.; Wang, Y.; Jiang, H. L. Metal-organic frameworks as platforms for catalytic applications. *Adv. Mater.* **2018**, 30, 1703663.

[15] Jiao, L; Jiang, H. L. Metal-organic-framework-based single-atom catalysts for energy applications. *Chem* **2019**, 5, 786–804.

[16] Meek, S. T.; Greathouse, J. A.; Allendorf, M. D. Metal–organic frameworks: A rapidly growing class of versatile nanoporous materials. *Adv. Mater.* **2011**, *23*, 249–267.

[17] Yang, S. J.; Cho, J. H.; Lee, K.; Kim, T.; Park, C. R. Concentration-driven evolution of crystal structure, pore characteristics, and hydrogen storage capacity of metal organic framework-5s: Experimental and computational studies. *Chem. Mater.* **2010**, *22*, 6138–6145.

[18] Stock, N.; Biswas, S. Synthesis of metal-organic frameworks (MOFs): Routes to various MOF topologies, morphologies, and composites. *Chem. Rev.* **2012**, *112*, 933–969.

[19] Ni, Z.; Masel, R. I. Rapid production of metal−organic frameworks via microwave-assisted solvothermal synthesis. *J. Am. Chem. Soc.* **2006**, *128*, 12394–12395.

[20] Ming, Y.; Kumar, N.; Siegel, D. J. Water adsorption and insertion in MOF-5. *ACS Omega* **2017**, *2*, 4921–4928.

[21] Kang, J. H.; Kim, T.; Choi, J.; Park, J.; Kim, Y. S.; Chang, M. S.; Jung, H.; Park, K. T.; Yang, S. J.; Park, C. R. Hidden second oxidation step of hummers method. *Chem. Mater.* **2016**, *28*, 756–764.

[22] Kim, Y. S.; Kang, J. H.; Kim, T.; Jung, Y.; Lee, K.; Oh, J. Y.; Pank, J.; Park, C. R. Easy preparation of readily self-assembled high-performance graphene oxide fibers. *Chem. Mater.* **2014**, *26*, 5549–5555.

[23] Oh, J. Y.; Yang, S. J.; Park, J. Y.; Kim, T.; Lee, K.; Kim, Y. S.; Han, H. N.; Park, C. R. Easy preparation of self-assembled high-density buckypaper with enhanced mechanical properties. *Nano Lett.* **2015**, *15*, 190–197.

[24] Oh, J. Y.; Kim, Y. S.; Jung, Y.; Yang, S. J.; Park, C. R. Preparation and exceptional mechanical properties of bone-mimicking size-tuned graphene oxide@carbon nanotube hybrid paper. *ACS Nano* **2016**, *10*, 2184–2192.

[25] Burtch, N. C.; Jasuja, H.; Walton, K. S. Water stability and adsorption in metal–organic frameworks. *Chem. Rev.* **2014**, *114*, 10575–10612.

[26] Song, F. Z.; Zhu, Q. L.; Yang, X. C.; Zhan, W. W.; Pachfule, P.; Tsumori, N.; Xu, Q. Metal–organic framework templated porous carbon-metal oxide/reduced graphene oxide as superior support of bimetallic nanoparticles for efficient hydrogen generation from formic acid. *Adv. Energy Mater.* **2018**, *8*, 1701416.

[27] Taylor, J. M.; Vaidhyanathan, R.; Iremonger, S. S.; Shimizu, G. K. H. Enhancing water stability of metal–organic frameworks via phosphonate monoester linkers. *J. Am. Chem. Soc.* **2012**, *134*, 14338–14340.

[28] Zhang, W.; Hu, Y. L.; Ge, J.; Jiang, H. L.; Yu, S. H. A facile and general coating approach to moisture/water-resistant metal–organic frameworks with intact porosity. *J. Am. Chem. Soc.* **2014**, *136*, 16978–16981.

[29] Xu, G. Y.; Nie, P.; Dou, H.; Ding, B.; Li, L. Y.; Zhang, X. G. Exploring metal organic frameworks for energy storage in batteries and supercapacitors. *Mater. Today* **2017**, *20*, 191–209.

[30] Greathouse, J. A.; Allendorf, M. D. The interaction of water with MOF-5 simulated by molecular dynamics. *J. Am. Chem. Soc.* **2006**, *128*, 10678–10679.

[31] Ming, Y.; Purewal, J.; Yang, J.; Xu, C. C.; Soltis, R.; Warner, J.; Veenstra, M.; Gaab, M.; Müller, U.; Siegel, D. J. Kinetic stability of MOF-5 in humid environments: Impact of powder densification, humidity level, and exposure time. *Langmuir* **2015**, *31*, 4988–4995.

[32] Rodríguez, N. A.; Parra, R.; Grela, M. A. Structural characterization, optical properties and photocatalytic activity of MOF-5 and its hydrolysis products: Implications on their excitation mechanism. *RSC Adv.* **2015**, *5*, 73112–73118.

[33] Yang, S. J.; Park, C. R. Preparation of highly moisture-resistant black-colored metal organic frameworks. *Adv. Mater.* **2012**, *24*, 4010–4013.

[34] Tranchemontagne, D. J.; Hunt, J. R.; Yaghi, O. M. Room temperature synthesis of metal-organic frameworks: MOF-5, MOF-74, MOF-177, MOF-199, and IRMOF-0. *Tetrahedron* **2008**, *64*, 8553–8557.

[35] Greer, H. F.; Liu, Y. H.; Greenaway, A.; Wright, P. A.; Zhou, W. Z. Synthesis and formation mechanism of textured MOF-5. *Cryst. Growth Des.* **2016**, *16*, 2104–2111.

[36] Huang, L. M.; Wang, H. T.; Chen, J. X.; Wang, Z. B.; Sun, J. Y.; Zhao, D. Y.; Yan, Y. S. Synthesis, morphology control, and properties of porous metal-organic coordination polymers. *Micropor. Mesopor. Mater.* **2003**, *58*, 105–114.

[37] Hausdorf, S.; Wagler, J.; Moβig, R.; Mertens, F. O. R. L. Proton and water activity-controlled structure formation in zinc carboxylate-based metal organic frameworks. *J. Phys. Chem. A* **2008**, *112*, 7567–7576.

[38] Thirumurugan, A.; Rao, C. N. R. 1,2-, 1,3- and 1,4-benzenedicarboxylates of Cd and Zn of different dimensionalities: Process of formation of the three-dimensional structure. *J. Mater. Chem.* **2015**, *15*, 3852–3858.

[39] Müller, M.; Turner, S.; Lebedev, O. I.; Wang, Y. M.; Van Tendeloo, G.; Fischer, R. A. Au@MOF-5 and Au/MO_x@MOF-5 (M = Zn, Ti; x = 1, 2): Preparation and microstructural characterisation. *Eur. J. Inorg. Chem.* **2011**, *2011*, 1876–1887.

[40] Chen, R. Z.; Hu, Y.; Shen, Z.; Chen, Y. L.; He, X.; Zhang, X. W.; Zhang, Y. Controlled synthesis of carbon nanofibers anchored with $Zn_xCo_{3-x}O_4$ nanocubes as binder-free anode materials for lithium-ion batteries. *ACS Appl. Mater. Interfaces* **2016**, *8*, 2591–2599.

[41] Han, S.; Lah, M. S. Simple and efficient regeneration of MOF-5 and HKUST-1 via acid–base treatment. *Cryst. Growth Des.* **2015**, *15*, 5568–5572.

[42] Tan, K.; Nijem, N.; Canepa, P.; Gong, Q. H.; Li, J.; Thonhauser, T.; Chabal, Y. J. Stability and hydrolyzation of metal organic frameworks with paddle-wheel SBUs upon hydration. *Chem. Mater.* **2012**, 24, 3153–3167.

[43] Du, J. H.; Pei, S. F.; Ma, L. P.; Cheng, H. M. 25th anniversary article: Carbon nanotube- and graphene-based transparent conductive films for optoelectronic devices. *Adv. Mater.* **2014**, *26*, 1958–1991.

[44] Jeong, Y. C.; Kim, J. H.; Nam, S.; Park, C. R.; Yang, S. J. Rational design of nanostructured functional interlayer/separator for advanced Li–S batteries. *Adv. Funct. Mater.* **2018**, *28*, 1707411.

[45] Shan, X. Y.; Wang, Y. Z.; Wang, D. W.; Li, F.; Cheng, H. M. Armoring graphene cathodes for high-rate and long-life lithium ion supercapacitors. *Adv. Energy Mater.* **2016**, *6*, 1502064.

[46] Liu, B.; Shioyama, H.; Akita, T.; Xu, Q. Metal-organic framework as a template for porous carbon synthesis. *J. Am. Chem. Soc.* **2008**, *130*, 5390–5391.

[47] Yang, S. J.; Kim, T.; Im, J. H.; Kim, Y. S.; Lee, K.; Jung, H.; Park, C. R. MOF-derived hierarchically porous carbon with exceptional porosity and

hydrogen storage capacity. *Chem. Mater.* **2012**, *24*, 464–470.
[48] Zhu, Q. L.; Xu, Q. Metal-organic framework composites, *Chem. Soc. Rev.* **2014**, *43*, 5468–5512.
[49] Fletcher, E. A. Solarthermal and solar quasi-electrolytic processing and separations: Zinc from zinc oxide as an example. *Ind. Eng. Chem. Res.* **1999**, 38, 2275–2282.
[50] Wu, M. C.; Lee, C. S. Synthesis and thermal decomposition of $Zn(tda)H_2O$ [tda = $S(CH_2COO)_2^{2-}$]. *Inorg. Chem.* **2006**, 45, 9634–9636.
[51] Zhao, S. L.; Yin, H. J.; Du, L.; He, L. C.; Zhao, K.; Chang, L.; Yin, G. P.; Zhao, H. J.; Liu, S. Q.; Tang, Z. Y. Carbonized nanoscale metal–organic frameworks as high performance electrocatalyst for oxygen reduction reaction. *ACS Nano* **2014**, *8*, 12660–12668.
[52] Yang, S. J.; Nam, S.; Kim, T.; Im, J. H.; Jung, H.; Kang, J. H.; Wi, S.; Park, B.; Park, C. R. Preparation and exceptional lithium anodic performance of porous carbon-coated ZnO quantum dots derived from a metal–organic framework. *J. Am. Chem. Soc.* **2013**, *135*, 7394–7397.
[53] Liang, Z. B.; Qu, C.; Xia, D. G.; Zou, R. Q.; Xu, Q. Atomically dispersed metal sites in MOF-based materials for electrocatalytic and photocatalytic energy conversion. *Angew. Chem., Int. Ed.* **2018**, *57*, 9604–9633.
[54] Yan, J.; Fan, Z. J.; Sun, W.; Ning, G. Q.; Wei, T.; Zhang, Q.; Zhang, R. F.; Zhi, L. J.; Wei, F. Advanced asymmetric supercapacitors based on $Ni(OH)_2$/graphene and porous graphene electrodes with high energy density. *Adv. Funct. Mater.* **2012**, *22*, 2632–2641.
[55] Fan, Z. J.; Yan, J.; Zhi, L. J.; Zhang, Q.; Wei, T.; Feng, J.; Zhang, M. L.; Qian, W. Z.; Wei, F. A three-dimensional carbon nanotube/graphene sandwich and its application as electrode in supercapacitors. *Adv. Mater.* **2010**, *22*, 3723–3728.
[56] Wu, Z. S.; Ren, W. C.; Wen, L.; Gao, L. B.; Zhao, J. P.; Chen, Z. P.; Zhou, G. M.; Li, F.; Cheng, H. M. Graphene anchored with Co_3O_4 nanoparticles as anode of lithium ion batteries with enhanced reversible capacity and cyclic performance. *ACS Nano* **2010**, *4*, 3187–3194.
[57] Poizot, P.; Laruelle, S.; Grugeon, S.; Dupont, L.; Tarascon, J. M. Nano-sized transition-metal oxides as negative-electrode materials for lithium-ion batteries. *Nature* **2000**, *407*, 496–499.
[58] Li, H.; Balaya, P.; Maier, J. Li-storage via heterogeneous reaction in selected binary metal fluorides and oxides. *J. Electrochem. Soc.* **2004**, *151*, A1878-A1885.
[59] Sun, J.; Lee, H. W.; Pasta, M.; Yuan, H. T.; Zheng, G. Y.; Sun, Y. M.; Li, Y. Z.; Cui, Y. A phosphorene-graphene hybrid material as a high-capacity anode for sodium-ion batteries. *Nat. Nanotechnol.* **2015**, *10*, 980–985.
[60] Sakaushi, K.; Lyalin, A.; Tominaka, S.; Taketsugu, T.; Uosaki, K. Two-dimensional corrugated porous carbon-, nitrogen-framework/metal heterojunction for efficient multielectron transfer processes with controlled kinetics. *ACS Nano* **2017**, *11*, 1770–1779.
[61] Wong, E. M.; Bonevich, J. E.; Searson, P. C. Growth kinetics of nanocrystalline ZnO particles from colloidal suspensions. *J. Phys. Chem. B* **1998**, *102*, 7770–7775.
[62] Chmiola, J.; Yushin, G.; Gogotsi, Y.; Portet, C.; Simon, P.; Taberna, P. L. Anomalous increase in carbon capacitance at pore sizes less than 1 nanometer. *Science* **2006**, *313*, 1760–1763.
[63] Feng, Y.; Zhang, Y. L.; Song, X. Y.; Wei, Y. Z.; Battaglia, V. S. Facile hydrothermal fabrication of ZnO–graphene hybrid anode materials with excellent lithium storage properties. *Sustainable Energy Fuels* **2017**, *1*, 767–779
[64] Yu, S. H.; Lee, D. J.; Park, M.; Kwon, S. G.; Lee, H. S.; Jin, A. H.; Lee, K. S.; Lee, J. E.; Oh, M. H.; Kang, K. et al. Hybrid cellular nanosheets for high-performance lithium-ion battery anodes. *J. Am. Chem. Soc.* **2015**, 137, 11954–11961.
[65] Sun, X.; Zhou, C. G.; Xie, M.; Sun, H. T.; Hu, T.; Lu, F. Y.; Scott, S. M.; George, S. M.; Lian, J. Synthesis of ZnO quantum dot/graphene nanocomposites by atomic layer deposition with high lithium storage capacity. *J. Mater. Chem. A* **2014**, *2*, 7319–7326.
[66] Kushima, A.; Liu, X. H.; Zhu, G.; Wang, Z. L.; Huang, J. Y.; Li, J. Leapfrog cracking and nanoamorphization of ZnO nanowires during *in situ* electrochemical lithiation. *Nano Lett.* **2011**, *11*, 4535–4541.
[67] Liu, J. P.; Li, Y. Y.; Huang, X. T.; Li, G. Y.; Li, Z. K. Layered double hydroxide Nano- and microstructures grown directly on metal substrates and their calcined products for application as Li-ion battery electrodes. *Adv. Funct. Mater.* **2008**, *18*, 1448–1458.
[68] Belliard, F.; Irvine, J. T. S. Electrochemical performance of ball-milled ZnO-SnO_2 systems as anodes in lithium-ion battery. *J. Power Sources* **2001**, *97–98*, 219–222.
[69] Zhang, C. Q.; Tu, J. P.; Yuan, Y. F.; Huang, X. H.; Chen, X. T.; Mao, F. Electrochemical performances of Ni-coated ZnO as an anode material for lithium-ion batteries. *J. Electrochem. Soc.* **2007**, *154*, A65–A69.
[70] Ahmad, M.; Shi, Y. Y.; Nisar, A.; Sun, H. Y.; Shen, W. C.; Wei, M.; Zhu, J. Synthesis of hierarchical flower-like ZnO nanostructures and their functionalization by Au nanoparticles for improved photocatalytic and high performance Li-ion battery anodes. *J. Mater. Chem.* **2011**, *21*, 7723–7729.
[71] Nadimpalli, S. P. V.; Sethuraman, V. A.; Dalavi, S.; Lucht, B.; Chon, M. J.; Shenoy, V. B.; Guduru, P. R. Quantifying capacity loss due to solid-electrolyte-interphase layer formation on silicon negative electrodes in lithium-ion batteries. *J. Power Sources* **2012**, *215*, 145–151.
[72] An, S. J.; Li, J. L.; Du, Z. J.; Daniel, C.; Wood III, D. L. Fast formation cycling for lithium ion batteries. *J. Power Sources* **2017**, *342*, 846–852.
[73] Xia, F.; Kwon, S.; Lee, W. W.; Liu, Z. M.; Kim, S.; Song, T.; Choi, K. J.; Paik, U.; Park, W. I. Graphene as an interfacial layer for improving cycling performance of Si nanowires in lithium-ion batteries. *Nano Lett.* **2015**, *15*, 6658–6664.
[74] Su, Q. M.; Dong, Z. M.; Zhang, J.; Du, G. H.; Xu, B. S. Visualizing the electrochemical reaction of ZnO nanoparticles with lithium by *in situ* TEM: Two reaction modes are revealed. *Nanotechnology* **2013**, *24*, 255705
[75] Balaya, P.; Li, H.; Kienle, L.; Maier, J. Fully reversible homogeneous and heterogeneous Li storage in RuO_2 with high capacity. *Adv. Funct. Mater.* **2003**, 13, 621–625.
[76] Chen, C. C.; Maier, J. Decoupling electron and ion storage and the path from interfacial storage to artificial electrodes. *Nat. Energy* **2018**, *3*, 102–108.
[77] Bekaert, E.; Balaya, P.; Murugavel, S.; Maier, J.; Ménétrier, M. ^{6}Li MAS NMR investigation of electrochemical lithiation of RuO_2: Evidence for an interfacial storage mechanism. *Chem. Mater.* **2009**, 21, 856–861.
[78] Kim, J. H.; Byeon, M.; Jeong, Y. C.; Oh, J. Y.; Jung, Y.; Fechler, N.; Yang, S. J.; Park, C. R. Morphochemical imprinting of melamine cyanurate mesocrystals in glucose-derived carbon for high performance lithium ion batteries. *J. Mater. Chem. A* **2017**, 5, 20635–20642.